JMEPEG (1992) 1:97-112

Finite-Element Simulation of Induction Heat Treatment

K.F. Wang, S. Chandrasekar, and Henry T.Y. Yang

An efficient finite-element procedure has been developed for the analysis of induction heat treatment problems involving nonisothermal phase changes. The finite-element procedure first simulates the magnetic field developed when currents flow through an induction coil by solving Maxwell's electromagnetic field equations; at the following step, it calculates the temperature distribution in the workpiece due to eddy currents induced by the magnetic field. The final stage of the simulation involves the determination of the distributions of residual stress, hardness, and microstructure in the workpiece. The finite-element analysis includes temperature-dependent material properties, changes in permeability of the workpiece at the Curie temperature, a mixed hardening rule to describe the material constitutive model, and the incorporation of time-temperature-transformation (*TTT*) diagram. The procedure was applied to the simulation of the induction hardening of 1080 steel bar. Firstly, the magnetic field and temperatures developed in the workpiece during (a) the induction heating of an infinitely long 1080 steel cylinder by a single encircling coil and (b) the induction heating of a semi-infinite half-space by a single coil suspended above it were calculated using the finite-element procedures. These were validated by comparing them with analytical solutions derived for these configurations using a Green's function method. Finally, to demonstrate the predictive capability and practical applicability of the current finite-element procedure, two examples pertaining to the induction heat treatment of an infinite 1080 steel bar of square cross section and a notched finite 1080 steel cylinder of circular cross section were analyzed to predict the magnetic field, temperature, and residual stress distributions. The current finite-element procedure could be used as a powerful design tool for linking induction heat treating parameters with the mechanical property attributes of the heat treated component.

1 Introduction

SUITABLE thermal or mechanical treatments will produce extensive rearrangement of atoms in metals and alloys and corresponding marked variations in physical, chemical, and mechanical properties. A widely used process, which relies on such a thermal treatment to produce the desired thermal mechanical properties, is the induction heat treatment or the induction hardening process, and this is the focus of the present study.

In the induction hardening process, the workpiece, which is made of an electrically conducting material, is passed through coils carrying an alternating electric current. The electromagnetic field produced by the current-carrying coils induces eddy currents in the workpiece, and consequently, the workpiece is heated resistively. The eddy currents in essence produce a spatial and time varying distribution of heat sources throughout the volume of the workpiece. After the workpiece has attained a suitable temperature distribution, the induction heating is stopped, and the workpiece is quenched in a bath or by means of a spray. The workpiece hardness and microstructure change during this heating and quenching cycle due to the phase transformations taking place in the workpiece material. Furthermore, residual stresses are also induced within the workpiece.[1]

An important question that often confronts heat treatment engineers is, "What should induction heating and quenching parameters be to obtain a desired distribution of hardness, microstructure, and residual stress in the workpiece at the end of the induction heat treatment process?" In the vast majority of industrial heat treatment applications, due to the lack of well validated computer simulation tools, this question is presently answered through an extensive series of experiments and trial and error. The objective of this study is to develop a comprehensive model of the induction heat treatment process for steels that incorporates the solutions for the electromagnetic field, the mathematical modeling of the phase transformations, and the heat transfer process occurring during the heating and quenching cycles, and thermal-elastic-plastic stress analysis. Such a model could enable induction heat treatment process parameters to be linked with component attributes such as microstructure, hardness, and residual stress.

K.F. Wang, Graduate Student, School of Aeronautics and Astronautics; **S. Chandrasekar,** Associate Professor of Industrial Engineering, and **Henry T.Y. Yang,** Professor of Aeronautics and Astronautics and Dean of Engineering, Purdue University, West Lafayette, Indiana.

2 Background

There have been several investigations into the simulation of various aspects of the induction heat treatment process. In 1967, Dodd and Deeds[2,3] obtained the electromagnetic field in an infinitely long cylinder of constant permeability when heated by a single circular coil and also under a coil suspended above a half-space of constant permeability. The contribution of Dodd and Deeds lay in the fact that they obtained a completely analytical solution for the magnetic vector potential. Finite-element methods were used by Donea *et al.*[4] and Chari[5] to obtain the electromagnetic vector potential for some axisymmetric and two-dimensional problems. More recently, Meunier *et al.*[6] calculated the electromagnetic field in some two-dimensional and axisymmetric configurations for different conditions of supply voltage and current applied to a coil using finite elements. All of these analyses did not go beyond a calculation of the electromagnetic field.

The problem of calculating the temperature distribution in an inductively heated workpiece was addressed by Baker[7] for a one-dimensional heat flow problem. The effect of permeability

changes occurring during phase transition and its effect on the temperature distribution during induction heating was partially addressed by Massé *et al.*[8] using a finite-element method. The induction heating handbook by Davies and Simpson[1] gives some empirically obtained temperature distributions in industrial heat treatment problems.

The calculation of residual stresses and hardness of inductively heated and quenched workpieces was carried out by Melander[9] for two specific cases: (a) the heating of an infinitely long cylinder by a uniform magnetic flux along its length, which is a one-dimensional problem, and (b) the induction heating of an infinitely long cylinder by a stationary single coil when the workpiece moved with a constant velocity past the coil. In both these examples, Melander did not carry out any electromagnetic field calculations, but assumed a field that had been well characterized for these two geometrical configurations. The assumed electromagnetic field had been derived for electrical and magnetic properties that were independent of temperature.

The above investigations and several others[10-12] indicated that, although there had been much effort toward modeling the individual phase of the induction heat treatment process, there was little work done toward integrating the various modeling aspects to carry through the modeling from the magnetic field parameters to the final workpiece properties. This gap in the literature motivated the present study.

In this study, the finite-element method was used as the principal analysis tool to model the magnetic field, the temperature distribution, and the stress field during the induction heat treatment process. The magnetic field simulations using the finite-element procedure were validated using two examples, for which analytical solutions were obtained in this study by using a Green's function method. The present finite-element simulation of the magnetic field incorporated the effect of permeability changes occurring in the workpiece at the Curie temperature. This simulation was linked with finite-element procedures for temperature and stress analyses developed by the authors in an earlier paper[12] for the quenching of metallic materials. Thus, the simulation of the entire induction heat treatment cycle was carried out.

Four induction heat treatment problems were analyzed to demonstrate the efficiency and capability of the present finite-element procedure. These were the induction heat treatment of (1) an infinitely long 1080 steel cylinder by a single coil, (2) a half-space by a single coil above it, (3) an infinitely long 1080 steel square bar encircled by an infinitely long coil, and (4) a finite 1080 steel circular notched bar. Unless otherwise stated, in all of these examples, the material properties of the workpiece were assumed to vary with temperature. The current density in the coil was selected for each example based on the criterion that the surface of the workpiece should reach at least the austenitizing temperature.

3 The Computational Model

The simulation of the induction heat treatment cycle consists of three parts: (1) analysis of the magnetic field generated by currents flowing in the induction coil and the calculation of the heat source induced by them in the work material, (2) temperature analysis of the induction heating and quenching processes, which are both coupled to the phase transformation process and require a nonlinear finite-element analysis, and (3) stress analysis based on the thermal loads generated from the temperature analysis. The computational formulation for each of these simulations is given in this section.

3.1 *Analysis of the Magnetic Field*

To obtain the heat sources generated within the material during the induction heating process, it is necessary to solve for the magnetic vector potential generated in the workpiece when a current flows through the induction coil. This requires a solution of Maxwell's equations describing the electromagnetic field with the appropriate boundary conditions. This is briefly reviewed below and then applied to the induction heating problem. Maxwell's equations for the magnetic field are:[13]

$$\nabla \times \mathbf{H} = \mathbf{J} + \frac{\partial \mathbf{D}}{\partial t}$$

$$\nabla \times \mathbf{E} = -\frac{\partial \mathbf{B}}{\partial t}$$

$$\nabla \cdot \mathbf{B} = 0$$

$$\nabla \cdot \mathbf{D} = \rho \qquad [1]$$

where **H**, **J**, **E**, **D**, **B**, and ρ are, respectively, the magnetic field strength, current density, electric field strength, electric displacement, magnetic flux density, and charge density. The medium (work material and/or air gap) is assumed to be linear and isotropic, but not homogeneous. The constitutive relations are:

$$\mathbf{B} = \mu \mathbf{H}$$

$$\mathbf{D} = \varepsilon \mathbf{E}$$

$$\mathbf{J} = \sigma \mathbf{E} \qquad [2]$$

where μ, ε, and σ are, respectively, the magnetic permeability, permittivity, and electrical conductivity of the medium.

It may be shown[2-4] from the second and third equations in Eq 1 that the most general electric and magnetic field can be expressed in terms of the magnetic vector and electric scalar potentials, $\mathbf{A}'$ and Φ, in the following manner:

$$\mathbf{B} = \nabla \times \mathbf{A}' \qquad [3]$$

$$\mathbf{J} = -\sigma \frac{\partial \mathbf{A}'}{\partial t} - \sigma \nabla \Phi \qquad [4]$$

The displacement currents, $\partial \mathbf{D}/\partial t$, on the right side of the first equation in Eq 1 can be neglected at the frequencies of interest to our induction heating problem.[2,4] When **B** and **J** are expressed in the above form, the second and third equations in Eq 1 are satisfied identically, and the equations for $\mathbf{A}'$ and Φ are then obtained by substituting Eq 3 and 4 in the first equation of Eq 1. This gives:

$$\nabla \times \left(\frac{1}{\mu} \nabla \times \mathbf{A}' \right) = -\sigma \frac{\partial \mathbf{A}'}{\partial t} + \mathbf{J}_0' \qquad [5]$$

where $\mathbf{J}_0' = -\sigma\nabla\Phi$ is the source current density. The current in the coil is assumed to be sinusoidal with a frequency ω, and therefore:

$$\mathbf{J}_0' = \mathbf{J}_0 e^{j\omega t} \quad [6]$$

Assuming that $\mathbf{A}'$ varies sinusoidally with time, $\mathbf{A}' = \mathbf{A}'' e^{j(\omega t+\phi)} = \mathbf{A}e^{j\omega t}$. Equation 5 then becomes:

$$\nabla \times \left(\frac{1}{\mu}\nabla \times \mathbf{A}\right) = -j\omega\sigma\mathbf{A} + \mathbf{J}_0 \quad [7]$$

or

$$\frac{1}{\mu}\nabla(\nabla \cdot \mathbf{A}) - \frac{1}{\mu}\nabla^2\mathbf{A} + \nabla\left(\frac{1}{\mu}\right) \times (\nabla \times \mathbf{A}) = -j\omega\sigma\mathbf{A} + \mathbf{J}_0$$

For induction heating problems, $\nabla \cdot \mathbf{A} = 0$,[3] and this leads to the following differential equation for the magnetic vector potential $\mathbf{A}$:

$$\frac{1}{\mu}\nabla^2\mathbf{A} - j\omega\sigma\mathbf{A} - \nabla\left(\frac{1}{\mu}\right) \times (\nabla \times \mathbf{A}) + \mathbf{J}_0 = 0 \quad [8]$$

For the axisymmetric case, the only nonzero component of the vector potential is $A_\theta(r,z)$. Dropping the θ, Eq 8 becomes:

$$\frac{1}{\mu}\left(\frac{\partial^2 A}{\partial r^2} + \frac{1}{r}\frac{\partial A}{\partial r} + \frac{\partial^2 A}{\partial^2 z} - \frac{A}{r^2}\right) - j\omega\sigma A + \frac{\partial(1/\mu)}{\partial r}\left(\frac{1}{r}\frac{\partial rA}{\partial r}\right) + \frac{\partial(1/\mu)}{\partial z}\frac{\partial A}{\partial z} + J_0 = 0 \quad [9]$$

For the two-dimensional Cartesian case:

$$\frac{1}{\mu}\left(\frac{\partial^2 A_x}{\partial x^2} + \frac{\partial^2 A_x}{\partial y^2}\right) - j\omega\sigma A_x - \frac{\partial(1/\mu)}{\partial y}\left(\frac{\partial A_y}{\partial x} - \frac{\partial A_x}{\partial y}\right) + J_{0x} = 0$$

$$\frac{1}{\mu}\left(\frac{\partial^2 A_y}{\partial x^2} + \frac{\partial^2 A_y}{\partial y^2}\right) - j\omega\sigma A_y + \frac{\partial(1/\mu)}{\partial x}\left(\frac{\partial A_y}{\partial x} - \frac{\partial A_x}{\partial y}\right) + J_{0y} = 0 \quad [10]$$

The variational formulation of the equations for the finite-element solution can now be derived by using the identity in Ref 4. It was assumed that the magnetic permeability, μ, is a constant within the domain D bounded by the surface S. For the axisymmetric case, the variational form is

$$\iiint_D \frac{1}{\mu}\nabla A \cdot \nabla\delta A dD + \iiint_D \left(\frac{1}{\mu r^2} + j\omega\sigma\right) A\delta A dD = \iiint_D J_0\delta A dD + \iint_S \frac{1}{\mu}\frac{\partial A}{\partial n}\delta A dS \quad [11]$$

For the two-dimensional case, the variational form is

$$\frac{1}{\mu}\iiint_D \left(\frac{\partial A}{\partial x}\frac{\partial}{\partial x}\delta A + \frac{\partial A}{\partial y}\frac{\partial}{\partial y}\delta A\right) dD + \iiint_D j\omega\sigma A\delta A dD = \iiint_D J_0\delta A dD + \iint_S \frac{1}{\mu}\frac{\partial A}{\partial n}\delta A dS \quad [12]$$

With finite-element discretization, the complex vector potential can be written in matrix form as:

$$A = [N]\bar{A} \quad [13]$$

$$\delta A = [N]\delta\bar{A} \quad [14]$$

where $[N]$ is the matrix for the shape function and $\bar{A}$ is the matrix representing the nodal values of the complex vector potential.

Substituting Eq 13 and 14 into Eq 11 and 12, the general form of the finite-element equation is obtained for each element:

$$\{[k]^e + \{l\}^e\}\{A\} = \{F^e\} \quad [15]$$

where for the axisymmetric case:

$$k_{ij}^e = \iint_{v^e} \frac{2\pi}{\mu}\left(\frac{\partial N_i}{\partial r}\frac{\partial N_j}{\partial r} + \frac{\partial N_i}{\partial z}\frac{\partial N_j}{\partial z}\right) rdrdz$$

$$l_{ij}^e = \iint_{v^e} 2\pi\left(\frac{1}{\mu r^2} + j\omega\sigma\right) N_i N_j \, rdrdz$$

$$F_i^e = \iint_{v^e} 2\pi J_0 N_i rdrdz + \int_{S^e} \frac{1}{\mu} N_i \frac{\partial A}{\partial n} dS$$

and for the two-dimensional Cartesian case:

$$k_{ij}^e = \iint_{v^e} \frac{1}{\mu}\left(\frac{\partial N_i}{\partial x}\frac{\partial N_j}{\partial x} + \frac{\partial N_i}{\partial y}\frac{\partial N_j}{\partial y}\right) dxdy$$

$$l_{ij}^e = \iint_{v^e} j\omega\sigma N_i N_j \, dxdy$$

$$F_i^e = \iint_{v^e} J_0 N_i dxdy + \int_{S^e} \frac{1}{\mu} N_i \frac{\partial A}{\partial n} dS$$

In the formulation, the permeability, μ, is assumed to be a constant within an element, but can vary from one element to another.

3.2 *Temperature Analysis*

The calculation of the temperatures induced within the workpiece during the induction heating and subsequent quenching cycle requires a solution of the heat equation with convection boundary conditions. The analysis is described in detail for the quenching process in an earlier paper,[12] but will be briefly reviewed here.

The transient heat conduction equation for a solid with an internal heat source is

$$\nabla(k\nabla T) + \dot{q} = \rho C_p \frac{\partial T}{\partial t} \quad [16]$$

where k, ρ, and C_p are, respectively, the thermal conductivity, density, and specific heat of the solid, and $\dot{q}$ is the rate of heat generation within the material.

During induction heating, eddy currents are induced in the workpiece by the externally applied electromagnetic field, and these currents generate sources of heat within the workpiece through resistive heating. The rate of heat generation at any given point within the solid during heating cycle is given by:[8]

$$\dot{q} = \frac{\sigma\omega^2 |\mathbf{A}|^2}{2} \quad [17]$$

where $|\mathbf{A}|$ is the absolute value of the complex magnetic vector potential at that point. During the quenching cycle, $\dot{q}$ is the internal heat source arising out of the enthalpy change produced by the phase transformations within the material.

The convective boundary conditions for the problem at the free surface of the workpiece are given by:

$$-k\nabla T = h(T)(T_\infty - T_s) \quad [18]$$

where $h(T)$ is a pseudoconvective heat transfer coefficient that includes both convection and radiation effects and is temperature dependent, and T_s and T_∞ are the temperatures of the solid surface and the surroundings, respectively.

Because the heat treatment of steels is of major concern in this study, a typical microstructure for steel will be composed of one or more of the following phases — austenite, ferrite, pearlite, cementite, bainite, and martensite. In the finite-element formulation, the material properties, P, of the resulting microstructure within an element were assumed to be a linear combination of the corresponding properties of each phase P_i weighted proportional to the volume fraction, F_i, of that phase present within the element. Any material property, P, of the solid is therefore written as:

$$P(F_i,T) = \sum_{i=1}^{6} P_i(t)F_i \quad [19]$$

The kinetics of the various diffusion transformations (that is nonmartensitic) were described in the formulation by the following Avrami-type of equation:[14,15]

$$F_i = 1 - \exp\left[-C_i(t)\theta^{N_i(T)}\right] \quad [20]$$

where $C_i(T)$ and $N_i(T)$ are material parameters that were calculated from the experimental isothermal transformation diagram for the material,[16] and θ is the transformation time. Scheil's principle, as described in Ref 17, was used to calculate the incubation period after which any transformation begins. When the summation of the ratios

$$\sum_{i=1} \frac{\Delta t_i}{\alpha_i(T_i)} = 1 \quad [21]$$

the transformation was assumed to begin. Here, $\alpha_i(T_i)$ is the time required at temperature T_i for the isothermal transformation to begin.

The fraction F_6 of martensite formed at any given temperature was assumed to be described by Koistinen-Marburger law:[18]

$$F_6 = [1 - \exp[-\alpha(M_s - T)]]\left(1 - \sum_{i=1}^{5} F_i\right) \quad [22]$$

with $\alpha = 1.10 \times 10^{-2}\text{K}^{-1}$ and M_s being the martensite start temperature.

Equations 19 through 22 describe the important details of the phase transformation process that were used in the finite-element formulation for the temperature analysis. For more details of this formulation, see Ref 12 and the references therein.

3.3 *Stress Analysis*

During induction heat treatment, the workpiece undergoes plastic deformation due to thermal stresses arising from the sharp temperature gradients. In Ref 12, a thermo-elastic-plastic model that incorporated temperature-dependent material properties was developed for the stress analysis of the quenching of steels. The same formulation was used in the stress analysis of the induction heat treatment problem described in this study. The formulation is briefly described; for greater detail, the reader is referred to Ref 12.

The total strain was assumed to be the sum of the elastic, plastic, and thermal strains and can therefore be written as:

$$\varepsilon_{ij} = \varepsilon_{ij}^e + \varepsilon_{ij}^p + \varepsilon_{ij}^t \quad [23]$$

In the present analysis, the von Mises yield function was used, and the plastic flow was assumed to be controlled by a mixed linear hardening rule. The yield function then becomes:

$$F = \frac{1}{2}(S_{ij} - \alpha_{ij})(S_{ij} - \alpha_{ij}) - \frac{1}{3}\sigma_y^2 \quad [24]$$

where S_{ij} and α_{ij} are, respectively, the components of the deviator stress and the coordinates of the center of the yield surface.

The stress-strain curve for the material was assumed to follow a linear hardening rule, with the yield stress corresponding to an accumulated plastic strain ε^p given by:

$$\sigma_y = \sigma_{y0} + (1 - \beta)H'\varepsilon^p \quad [25]$$

where σ_{y0}, ε^p, and H', respectively, are the initial yield stress, accumulated plastic strain, and plastic modulus. β is a weighting factor that takes on values between 0 (isotropic hardening) and 1 (kinematic hardening).

In the analysis of induction heat treatment problems where the thermal loading at every point is cyclic over one cycle, a combination of isotropic and kinematic hardening (mixed hardening) is preferable. In a mixed hardening model, the movement of the center of the yield surface can be obtained from Prager's rule as:

$$d\alpha_{ij} = \frac{2}{3}\beta H' d\varepsilon_{ij}^p \quad [26]$$

The stress increment for these constitutive equations and plastic yield criterion was derived in an earlier paper[12] by the authors as:

$$d\sigma_{ij} = 2G de_{ij} + \delta_{ij} K(d\varepsilon_{kk} - d\varepsilon^t_{kk}) - \frac{2G(S_{ij} - \alpha_{ij})(S_{kl} - \alpha_{kl})d\varepsilon_{kl}}{W} + \left(S_{ij} - \frac{(S_{ij} - \alpha_{ij})(S_{kl} - \alpha_{kl})S_{kl}}{W}\right)\frac{dG}{G} + \frac{2\sigma_e \frac{\partial \sigma_y}{\partial T} dT}{3W}(S_{ij} - \alpha_{ij}) + \frac{1}{3}\delta_{ij}\sigma_{kk}\frac{dK}{K} \quad [27]$$

where

$$W = \frac{2}{3}\sigma_e^2\left(1 + \frac{H'}{3G}\right)$$

G and K are, respectively, the shear modulus and bulk modulus of the material. The effective stress σ_e in the material is given by:

$$\sigma_e^2 = \frac{3}{2}(S_{ij} - \alpha_{ij})(S_{ij} - \alpha_{ij}) \quad [28]$$

4 Applications

4.1 *Induction Heat Treatment of an Infinitely Long 1080 Steel Cylinder by a Single Coil*

The induction heat treatment of a circular 1080 carbon steel cylinder 40 mm in diameter was simulated. The cylinder was assumed to be initially at a uniform temperature of 25 °C. It was then heated by a circular induction coil having a square cross section 4 by 4 mm. Figure 1 shows the configuration of the cylinder and the coil and the finite-element mesh used in the simulation. The current density in the coil was assumed to be 7×10^9 A/m^2 and varying sinusoidally at a frequency of 60 Hz. The values of relative permeability and Curie temperature for 1080 steel were 90 and 725 °C, respectively. A relative permeability of 90 indicates that the absolute permeability of 1080 carbon steel is 90 times that of air. During the heating cycle, the energy losses due to convection at the free surfaces of the workpiece are typically small compared with the heat generated by the eddy currents and hence was neglected. The variation of the various thermal, physical, and mechanical properties of 1080 steel with temperature were taken from Ref 19 and 20, and these values were used in all the computations unless otherwise stated.

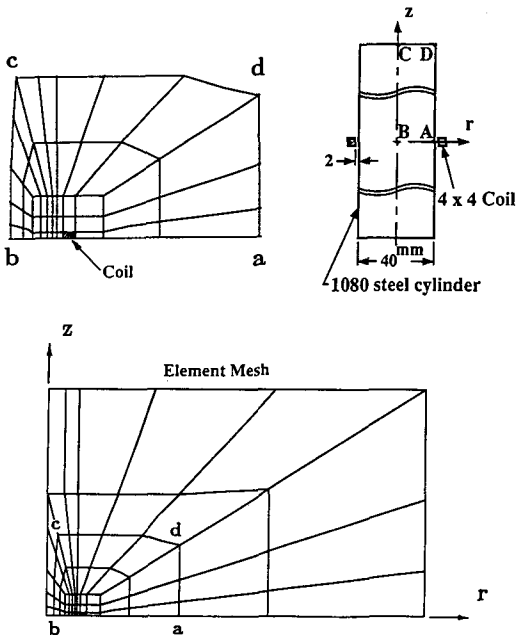

Fig. 1 Finite-element modeling for the induction heat treatment of an infinitely long 1080 steel cylinder encircled by a coil.

To verify the finite-element program, closed form solutions were derived for the magnetic vector potential and the temperature within the workpiece during the initial stages of induction heating. These solutions were obtained using a Green's function method originally proposed by Dodd and Deeds[2] for the induction heat treatment of an infinitely long cylinder. Dodd and Deeds obtained the magnetic vector potential within a two-conductor cylinder rod, *i.e.*, a rod composed of two coaxial cylinders having different electrical conductivities σ_1 and σ_2 (see Fig. 2), when heated by a circular coil that was infinitesimally thin. Such a coil is referred to as a delta-function coil. The derived potential for the delta-function coil is referred to as the Green's function for the vector potential. However, in their derivation, the permeability of two-conductor workpiece was assumed to be constant throughout, and the permeability of the air gap was also assumed to be the same as that of the workpiece. In practice, this is not the case. From the Green's function for the vector poten-

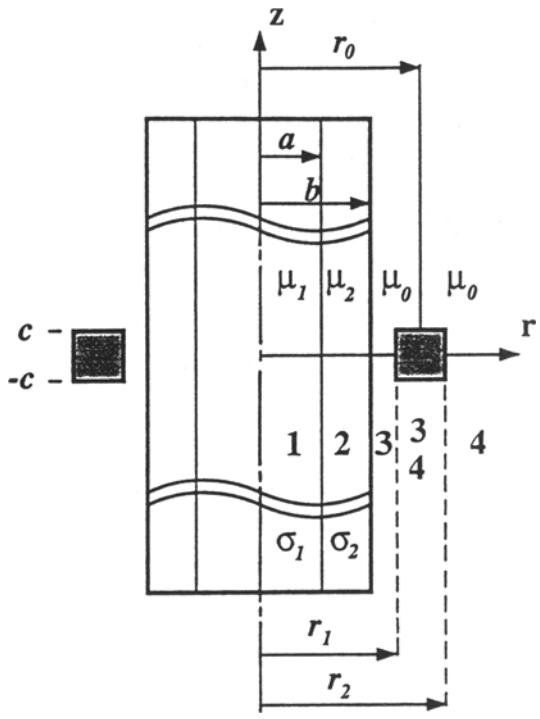

Fig. 2 Induction heating of a two-conductor rod encircled by one coil.

tial, Dodd and Deeds[2,3] obtained in the usual manner the vector potential in the two-conductor workpiece when heated by a circular coil having a finite square cross section.

In the present study, the Green's function analysis of Dodd and Deeds was extended to obtain the vector potential in a two-conductor rod (see Fig. 2), in which the coaxial cylinders have not only different electrical conductivities σ_1 and σ_2, but also different permeabilities μ_1 and μ_2. Also, the air gap permeability was assumed to be equal to μ_0, different from μ_1 and μ_2. This model represents the essential features of a typical induction heat treatment problem including the Curie phenomenon. For example, when a cylinder is inductively heated by a circular coil as in Fig. 2, the region near the surface is heated faster than the interior, and when the near surface regions reach the Curie temperature, they undergo a magnetic phase transition resulting in a drastic decrease in the permeability. Typically, the permeability at and above the Curie temperature of the workpiece material would be essentially the same as that of air. Thus, the model shown in Fig. 2 would represent a cylinder whose interior over a region of radius a is below the Curie temperature and has permeability μ_1, whereas the surface regions over a thickness of $(b-a)$ are above the Curie temperature and have a permeability of μ_2.

The governing differential equation in cylindrical coordinates for the magnetic vector potential $A^{(i)}$ in region i of the cylinder is

$$\frac{\partial^2 A^{(i)}}{\partial r^2}+\frac{1}{r}\frac{\partial A^{(i)}}{\partial r}+\frac{\partial^2 A^{(i)}}{\partial z^2}-\frac{A^{(i)}}{r^2}-j\omega\mu_i\sigma_i=0 \qquad [29]$$

where μ_i and σ_i are, respectively, the permeability and electrical conductivity of the workpiece in the region of interest. For the geometry shown in Fig. 2 and for a delta-function coil of strength J_0, the boundary conditions are

$$A^{(1)}(a,z-z_0)=A^{(2)}(a,z-z_0)$$

$$\frac{1}{\mu_1}\frac{\partial}{\partial r}A^{(1)}(a,z-z_0)=\frac{1}{\mu_2}\frac{\partial}{\partial r}A^{(2)}(a,z-z_0)$$

$$A^{(2)}(b,z-z_0)=A^{(3)}(b,z-z_0)$$

$$\frac{1}{\mu_2}\frac{\partial}{\partial r}A^{(2)}(b,z-z_0)=\frac{1}{\mu_0}\frac{\partial}{\partial r}A^{(3)}(b,z-z_0)$$

$$A^{(3)}(r_0,z-z_0)=A^{(4)}(r_0,z-z_0)$$

$$\frac{1}{\mu_0}\frac{\partial}{\partial r}A^{(3)}(r_0,z-z_0)=\frac{1}{\mu_0}\frac{\partial}{\partial r}A^{(4)}(r_0,z-z_0)+J_0\delta(z-z_0) \qquad [30]$$

The solution of the vector potential for these boundary conditions, which is the Green's function, is given in Appendix 1. This was obtained by solving the differential equation using the method of separation of variables. For a given current density applied to coils of finite cross-sectional area, the solutions for the vector potential in each region of Fig. 2 were obtained by integrating the Green's function over the cross-sectional area. This yielded:

$$A^{(1)}(r,z)=\frac{\mu_0 J_0}{\pi}\int_0^\infty C_1(\alpha)F(\alpha,r_1,r_2)I_1(\alpha_1 r)Z(\alpha,z)d\alpha$$

$$A^{(2)}(r,z)=\frac{\mu_0 J_0}{\pi}\int_0^\infty [C_2(\alpha)I_1(\alpha_2 r)+D_2(\alpha)K_1(\alpha_2 r)]F(\alpha,r_1,r_2)Z(\alpha,z)d\alpha$$

$$A^{(3)}(r,z)=\frac{\mu_0 J_0}{\pi}\int_0^\infty [I_1(\alpha r)+D_3(\alpha)K_1(\alpha r)]F(\alpha,r_1,r_2)Z(\alpha,z)d\alpha$$

$$A^{(4)}(r,z)=\frac{\mu_0 J_0}{\pi}\int_0^\infty [D_3(\alpha)F(\alpha,r_1,r_2)+G(\alpha,r_1,r_2)]K_1(\alpha r)Z(\alpha,z)d\alpha$$

$$A^{(3)(4)}(r,z)=\frac{\mu_0 J_0}{\pi}\int_0^\infty [I_1(\alpha r)+D_3(\alpha)K_1(\alpha r)]F(\alpha,r,r_2)Z(\alpha,z)d\alpha+\frac{\mu_0 J_0}{\pi}\int_0^\infty [D_3(\alpha)F(\alpha,r_1,r)+G(\alpha,r_1,r)]K_1(\alpha r)Z(\alpha,z)d\alpha \qquad [31]$$

where J_0 is the source current density in the coil:

$$D(\alpha)=[\frac{1}{\mu_{20}}\alpha_2 bI_0(\alpha_2 b)K_1(\alpha b)+\alpha bI_1(\alpha_2 b)K_0(\alpha b)+\left(1-\frac{1}{\mu_{20}}\right)I_1(\alpha_2 b)K_1(\alpha b)]\cdot[\frac{1}{\mu_{12}}\alpha_1 aK_1(\alpha_2 a)I_0(\alpha_1 a)+\alpha_2 aK_0(\alpha_2 a)I_1(\alpha_1 a)+\left(1-\frac{1}{\mu_{12}}\right)K_1(\alpha_2 a)I_1(\alpha_1 a)]-[-\frac{1}{\mu_{20}}\alpha_2 bK_0(\alpha_2 b)K_1(\alpha b)+\alpha bK_1(\alpha_2 b)K_0(\alpha b)+\left(1-\frac{1}{\mu_{20}}\right)K_1(\alpha_2 b)\,K_1(\alpha b)]\cdot[\frac{1}{\mu_{12}}\alpha_1 aI_1(\alpha_2 a)I_0(\alpha_1 a)-\alpha_2 aI_0(\alpha_2 a)I_1(\alpha_1 a)+\left(1-\frac{1}{\mu_{12}}\right)I_1(\alpha_2 a)I_1(\alpha_1 a)]$$

$$\mu_{12}=\frac{\mu_1}{\mu_2}$$

$$\mu_{20}=\frac{\mu_2}{\mu_0}$$

$$\alpha_i=\sqrt{\alpha^2+j\omega\mu_i\sigma_i}$$

$$C_1(\alpha)=\frac{1}{D(\alpha)}$$

$$C_2(\alpha) = \frac{1}{D(\alpha)}\left[\frac{1}{\mu_{12}}\alpha_1 a K_1(\alpha_2 a) I_0(\alpha_1 a) + \alpha_2 a K_0(\alpha_2 a) I_1(\alpha_1 a) + \left(1 - \frac{1}{\mu_{12}}\right) K_1(\alpha_2 a) I_1(\alpha_1 a)\right]$$

$$D_2(\alpha) = \frac{-1}{D(\alpha)}\left[\frac{1}{\mu_{12}}\alpha_1 a I_1(\alpha_2 a) I_0(\alpha_1 a) - \alpha_2 a I_0(\alpha_2 a) I_1(\alpha_1 a) + \left(1 - \frac{1}{\mu_{12}}\right) I_1(\alpha_2 a) I_1(\alpha_1 a)\right]$$

$$D_3(\alpha) = \frac{1}{K_1(\alpha b)} \cdot \left\{\frac{I_1(\alpha_2 b)}{D(\alpha)}\left[\frac{1}{\mu_{12}}\alpha_1 a K_1(\alpha_2 a) I_0(\alpha_1 a) + \alpha_2 a K_0(\alpha_2 a) I_1(\alpha_1 a) + \left(1 - \frac{1}{\mu_{12}}\right) K_1(\alpha_2 a) I_1(\alpha_1 a)\right] - \frac{K_1(\alpha_2 b)}{D(\alpha)}\left[\frac{1}{\mu_{12}}\alpha_1 a I_1(\alpha_2 a) I_0(\alpha_1 a) - \alpha_2 a I_0(\alpha_2 a) I_1(\alpha_1 a) + \left(1 - \frac{1}{\mu_{12}}\right) I_1(\alpha_2 a) I_1(\alpha_1 a)\right] - I_1(\alpha b)\right\}$$

$$F(\alpha, r_1, r_2) = \int_{r_1}^{r_2} r_0 K_1(\alpha r_0) dr_0$$

$$G(\alpha, r_1, r_2) = \int_{r_1}^{r_2} r_0 I_1(\alpha r_0) dr_0$$

$$Z(\alpha, z) = \frac{1}{\alpha}[\sin \alpha(c - z) + \sin \alpha(c + z)]$$

and K_0, K_1, I_0, and I_1 are the appropriate modified Bessel functions in the usual notation.

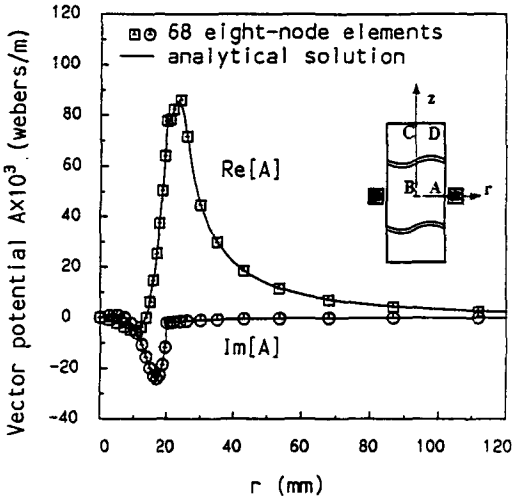

Fig. 3 Real and imaginary components of the vector potential along a radial direction from point B, assuming the permeability of the solid constant everywhere.

A closed form solution for the temperature distribution in the infinitely long rod with an internal heat source can also be obtained using a Green's function method,[21] in which no heat is assumed lost over the cylinder surfaces. As mentioned earlier, this is a reasonable model for the heating stage of the induction heat treatment process. The governing equation and boundary conditions are

$$\frac{\partial^2 T}{\partial r^2} + \frac{1}{r}\frac{\partial T}{\partial r} + \frac{\partial^2 T}{\partial z^2} + \frac{\dot{q}(r', z')}{K} = \frac{1}{\alpha}\frac{\partial T}{\partial t} \qquad [32]$$

$$BCs \begin{cases} \dfrac{\partial T}{\partial r} = 0 & r = 0, r = b \\ \dfrac{\partial T}{\partial z} = 0 & z = 0 \end{cases}$$

$$IC \quad T = T_0 \quad t = 0 \qquad [33]$$

where α is the thermal diffusivity and T_0 is the initial temperature.

The Green's function for this problem, *i.e.*, the solution for the temperature when a delta-function heat source is described over a circle, can be obtained as:[21]

$$G(r, z, t \mid r', z', \tau) = \frac{4}{\pi b^2}\int_0^\infty \cos(\eta z') \cos(\eta z) e^{-\alpha\eta^2(t-\tau)} d\eta + \frac{4}{\pi b^2}\sum_{m=2}^{\infty} \frac{1}{[J_0(\beta_m b)]^2}\int_0^\infty \cos(\eta z') \cos(\eta z) J_0(\beta_m r') J_0(\beta_m r) e^{-\alpha(\beta_m^2 + \eta^2)(t-\tau)} d\eta \qquad [34]$$

where β_m are roots of $J_1(\beta_m b) = 0$, and $J_0(x)$ and $J_1(x)$ are the Bessel function of the first kind. The transient temperature solution for induction heating is then:

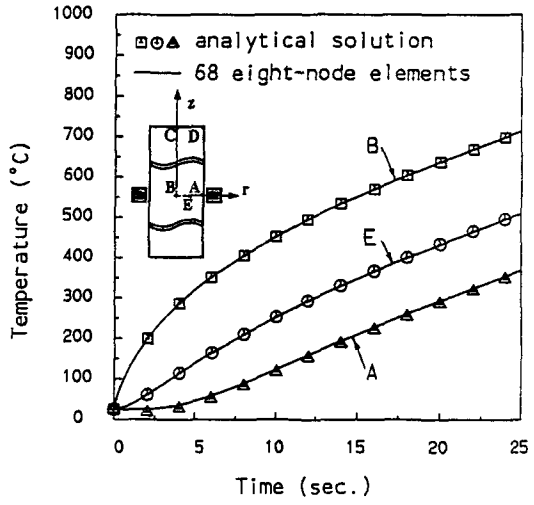

Fig. 4 Temperature histories at three points within the cylinder during the induction heating process, assuming the material properties constant throughout the workpiece.

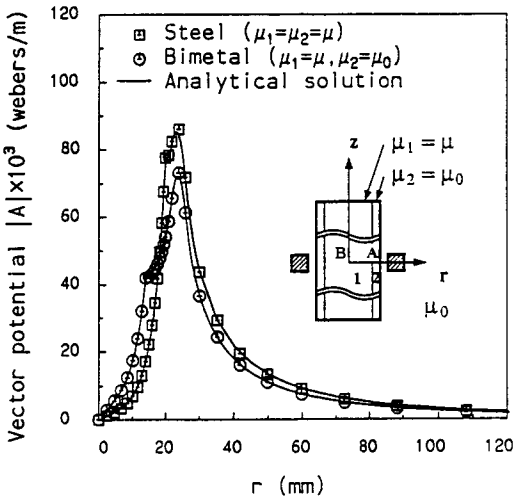

Fig. 5 Magnitude of the vector potential along a radial direction from point B for steel and a two-conductor bimetal.

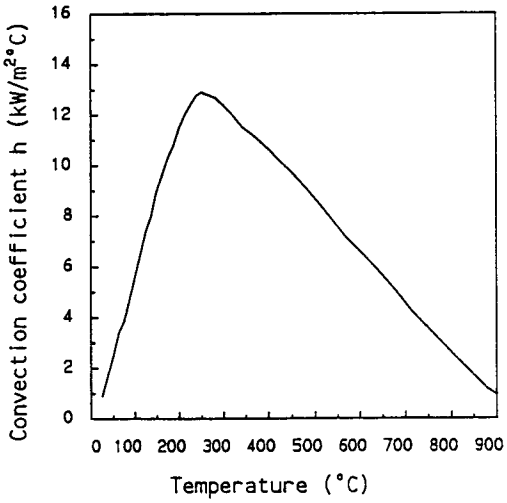

Fig. 6 Convection coefficient as a function of temperature for 6% UCON quenchant.

$$T(r,z,t) = T_0 + \frac{\alpha}{k}\int_0^b\int_0^\infty \frac{4}{\pi b^2}\int_0^\infty \frac{\cos(\eta z')\cos(\eta z)(1-e^{-\alpha\eta^2 t})}{\alpha\eta^2}$$

$$\dot{q}(r',z')d\eta r'dr'dz' + \frac{\alpha}{k}\int_0^b\int_0^\infty \sum_{m=2}^{\infty}\frac{4}{\pi b^2[J_0(\beta_m b)]^2}$$

$$\int_0^\infty \frac{\cos(\eta z')\cos(\eta z)J_0(\beta_m r')J_0(\beta_m r)}{\alpha(\beta_m^2+\eta^2)}$$

$$\cdot\left[1-e^{-\alpha(\beta_m^2+\eta^2)t}\right]d\eta\dot{q}(r',z')r'dr'dz' \qquad [35]$$

where $\dot{q}(r',z') = \sigma\omega^2[A(r',z')A^*(r',z')]/2$ is the magnitude of the heat source generated by the eddy currents in the workpiece.

The analytical solutions for the vector potential and the temperature within the infinite cylinder that were obtained using the Green's function technique were compared with the finite-element simulation results. A finite-element mesh with 68 isoparametric eight-node elements (Fig. 1) was used to model half of the space including the cylinder, coil, and the air gap. The comparison between the Green's function solutions and the finite-element results were carried out for two cases.

In the first case, the workpiece material (1080 steel) was assumed to have constant values of 3×10^6 mho/m, 7500 kg/m^3, 650 J/kg · K, and 35 W/m · K, respectively, for the electrical conductivity, density, specific heat, and thermal conductivity. The relative permeability of the 1080 steel workpiece was assumed to be 90, whereas the air gap had a relative permeability of 1 and an absolute permeability of $4\pi \times 10^{-7}$ H/m. Figure 3 shows the distributions of the real and complex parts of the vector potential along a radial line from point B (see inset of Fig. 3) that were calculated using the Green's function method (analytical solution) and finite-element analysis. The temperature histories at three different points in the cylinder were obtained analytically and numerically for the initial stage of heating and are shown in Fig. 4. From these figures, it is evident that there is excellent agreement between the finite-element and analytical solutions for the vector potential and the temperature.

The second comparison between the finite-element and analytical solutions for the vector potential was carried out for the case of a two-conductor cylindrical rod (see Fig. 2 and inset of Fig. 5). In the inset of Fig. 5, the relative permeabilities of the inner (Region 1) and outer (Region 2) regions of the rod are assumed to be $\mu_1 = 90$ (1080 steel) and $\mu_2 = 1$, respectively. The air gap was assumed to have a relative permeability of $\mu_0 = 1$. This configuration corresponds to a 1080 steel cylinder whose outer region has reached the Curie temperature. From Fig. 5, it is clear that there is excellent agreement between the finite-element and analytical solutions for the vector potential for this configuration also. For reference purposes, the finite-element and analytical solutions for vector potential obtained in the previous case, *i.e.*, for a 1080 steel cylinder having a constant permeability of $\mu_1 = \mu_2 = \mu$ are also shown in Fig. 5. The effect of including the Curie phase transition in the model is observed by comparing the two curves in Fig. 5.

Three finite-element meshes (68, 94, and 144 elements, respectively) were used to model this problem to observe the convergence of results. It was found that all three of the meshes generated practically the same results, suggesting that the solution had converged at the 68-element level and stayed convergent as the meshes were successively refined. Although meshes slightly coarser than 68 elements could still generate the same solutions, the resulting curves were no longer smooth when plotted by computer. Thus, the 68-element mesh, as shown in Fig. 1, was used to solve this problem.

Figures 6 to 11 describe the finite-element simulation of the complete induction heat treatment process for the infinitely long cylinder encircled by one coil. For this simulation, the 40-mm-diameter 1080 steel cylinder was inductively heated for 70 sec at the current density specified earlier, then air cooled for 5 sec and subsequently quenched in a 6% UCON quenchant assumed to be at a room temperature of 25 °C. The convection heat transfer coefficient for 6% UCON is given in Fig. 6, whereas that of air

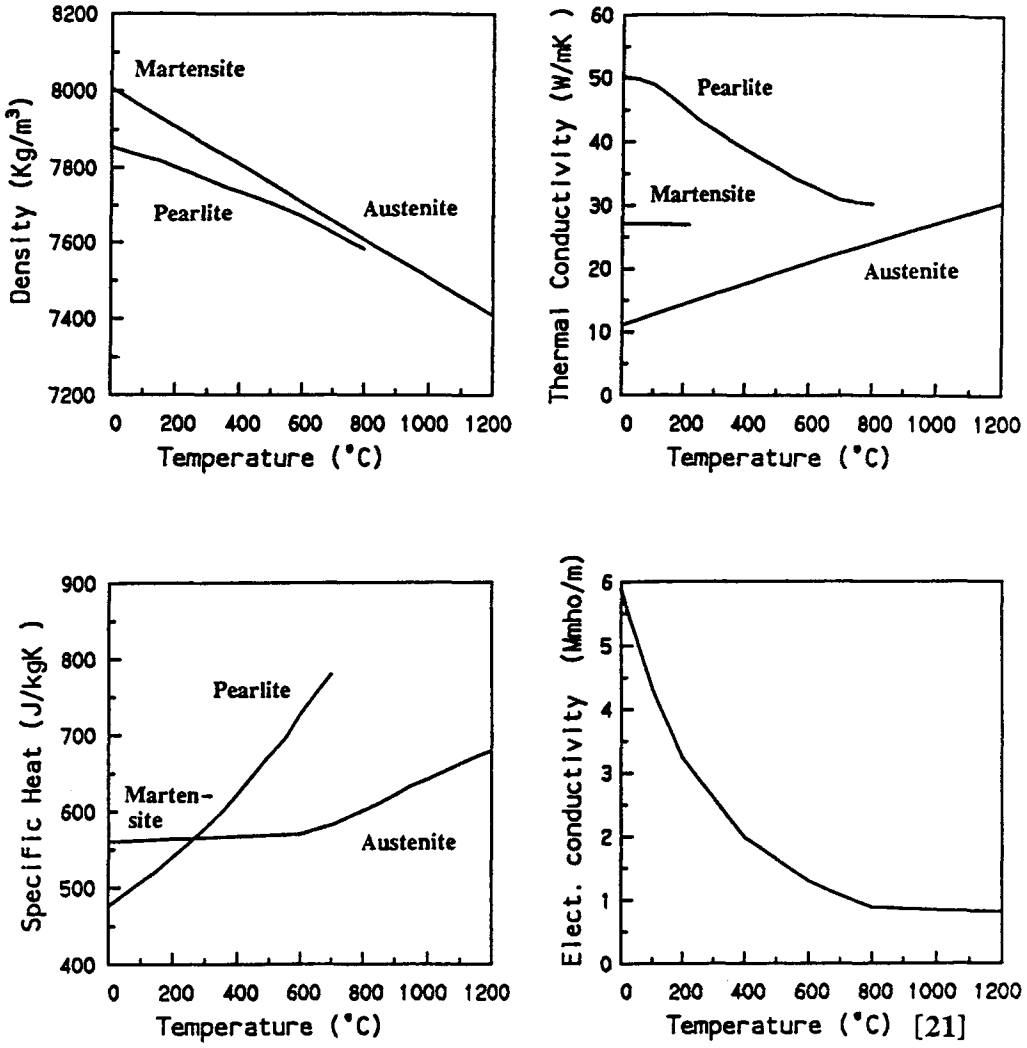

Fig. 7 Physical properties of 1080 steel as a function of temperature.

was assumed to be 30 W/m^2 · C. The physical and mechanical properties were assumed to be temperature dependent, as shown in Fig. 7 and 8.

In Fig. 9, it is shown that the temperature of point A on the cylinder surface shows a discontinuity in its time derivative at the Curie temperature of 725 °C. A similar feature is observed in the temperature history of point B at the same time. The other noticeable discontinuities in the time derivatives of the temperature in Fig. 9 correspond to the onset of air cooling and UCON quenching, and the occurrence of phase transformations within the workpiece. The stress histories and the residual stresses at selected points in the cylinder are shown in Fig. 10 and 11, respectively. Both the hoop and the axial residual stresses are compressive to a depth of about 4 mm from the surface (see Fig. 11), whereas at the center of the cylinder, the residual stress state is somewhat similar to hydrostatic tension. These tensile residual stresses at the center are potentially critical to not only dictating failure of the cylinder, but also in determining limits on the maximum allowable quenching rates.

4.2 *Induction Heat Treatment of a Half-Space by a Single Coil Above It*

Figure 12 shows a schematic of the induction heating of a semi-infinite solid (half-space) by a single circular coil placed above the surface. The cross section of the coil was the same as that used in the previous example. Also shown in Fig. 12 is the finite-element mesh used to simulate the heat treatment process for obtaining the distributions of magnetic vector potential, temperature, and residual stress in the workpiece, which was 1080 carbon steel. The mesh consisted of 132 isoparametric eight-node elements for the entire space. As in the previous example,

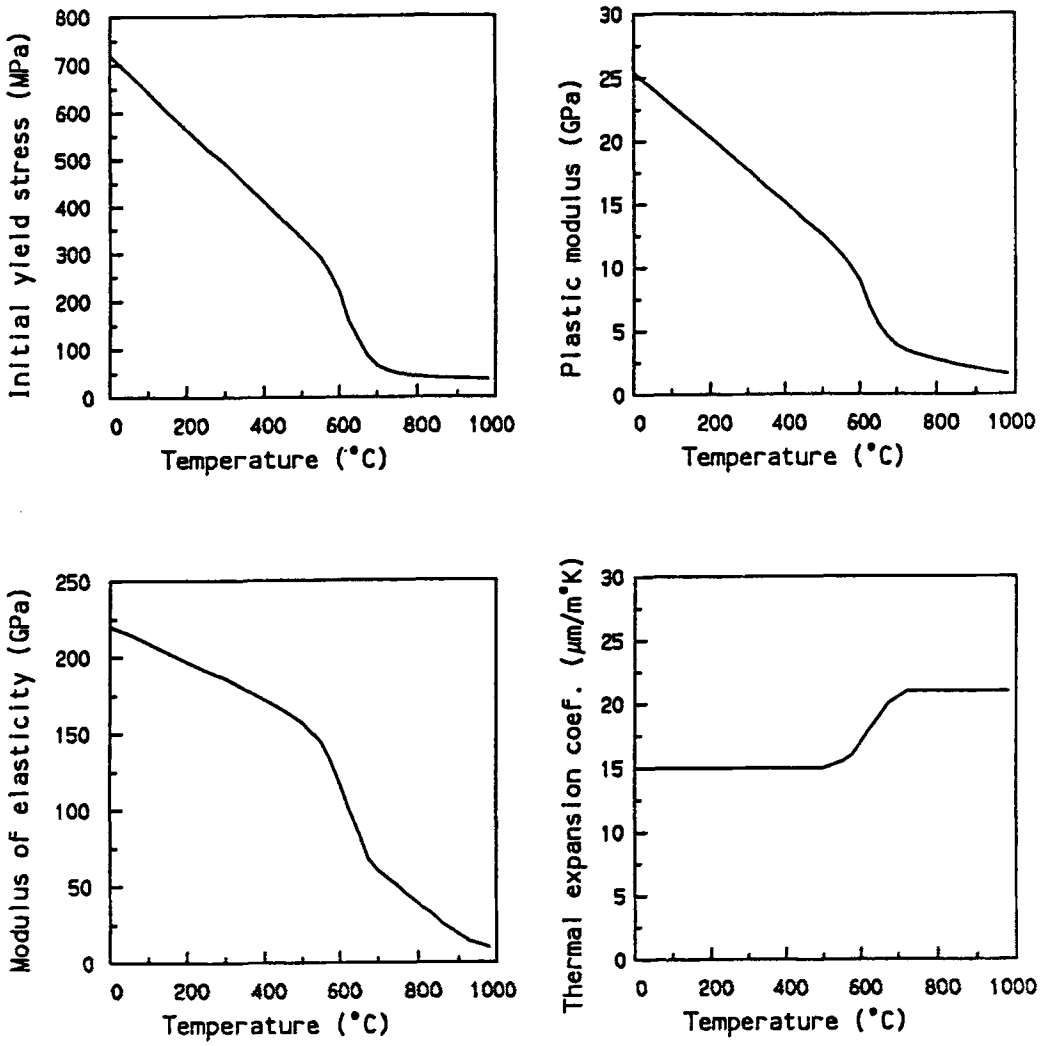

Fig. 8 Mechanical properties of 1080 steel as a function of temperature.

the solutions for magnetic vector potential and the temperature distribution in the workpiece during the induction heating process were also derived in closed form by using a Green's function method and were compared with the corresponding finite-element results.

Appendix 2 gives the Green's functions for the magnetic vector potential in different parts of the coil/workpiece system shown in Fig. 12. The Green's functions were obtained as the solutions for a circular delta-function coil located above the surface of the 1080 steel workpiece; the relative magnetic permeability of the 1080 steel was assumed to be 90. In the derivation, all the thermophysical and electrical properties of the workpiece were assumed to be constant and independent of temperature.

The Green's functions of Appendix 2 can be integrated over the coil cross section and the current density to obtain the vector potentials for this problem:

$$A^{(1)}(r,z) = \frac{\mu_0 J_0}{2} \int_0^\infty \frac{1}{\alpha^3} F(r_1,r_2) J_1(\alpha r)[(e^{\alpha l_2} - e^{\alpha l_1}) + w\,(e^{-\alpha l_1} - e^{-\alpha l_2})]e^{-\alpha z} d\alpha$$

$$A^{(2)}(r,z) = \frac{\mu_0 J_0}{2} \int_0^\infty \frac{1}{\alpha^3} F(r_1,r_2) J_1(\alpha r)(e^{-\alpha l_1} - e^{-\alpha l_2})(e^{\alpha z} + we^{-\alpha z}) d\alpha$$

$$A^{(1,2)}(r,z) = \frac{\mu_0 J_0}{2} \int_0^\infty \frac{1}{\alpha^3} F(r_1,r_2) J_1(\alpha r) \cdot ([(e^{\alpha z} - e^{\alpha l_1}) + w(e^{-\alpha l_1} - e^{-\alpha z})]e^{-\alpha z} + (e^{-\alpha z} - e^{-\alpha l_2})(e^{\alpha z} + we^{-\alpha z})) d\alpha$$

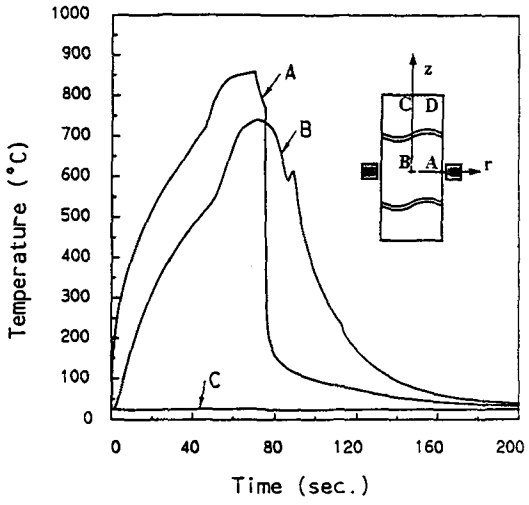

Fig. 9 Temperature histories at three points within the infinitely long cylinder during the heat treatment process, assuming that the material properties for this simulation are temperature dependent[19] with the Curie temperature being 725 °C.

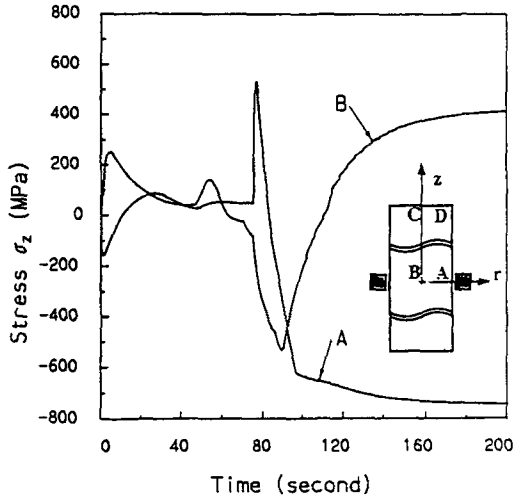

Fig. 10 Histories of axial stresses at the center B and point A of the cylinder.

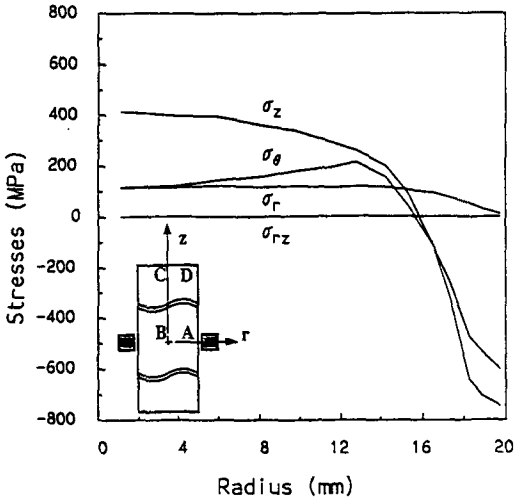

Fig. 11 Distribution of residual stresses in the radial direction from point B to point A.

$$A^{(3)}(r,z) = \frac{\mu_0 J_0}{2}\int_0^\infty \frac{1}{\alpha^3} F(r_1,r_2) J_1(\alpha r)$$

$$(e^{-\alpha l_1} - e^{-\alpha l_2})(1+w)e^{\alpha_1 z} d\alpha \qquad [36]$$

where $A^{(i)}(r,z)$ is the potential in region i of the coil/workpiece system.

$$F(r_1,r_2) = \alpha^2 \int_{r_1}^{r_2} r_0 J_1(\alpha r_0) dr_0$$

$$w = \frac{\mu_r \alpha - \alpha_1}{\mu_r \alpha + \alpha_1}$$

$$\alpha_1 = \sqrt{\alpha^2 + j\omega\mu_1\sigma_1}$$

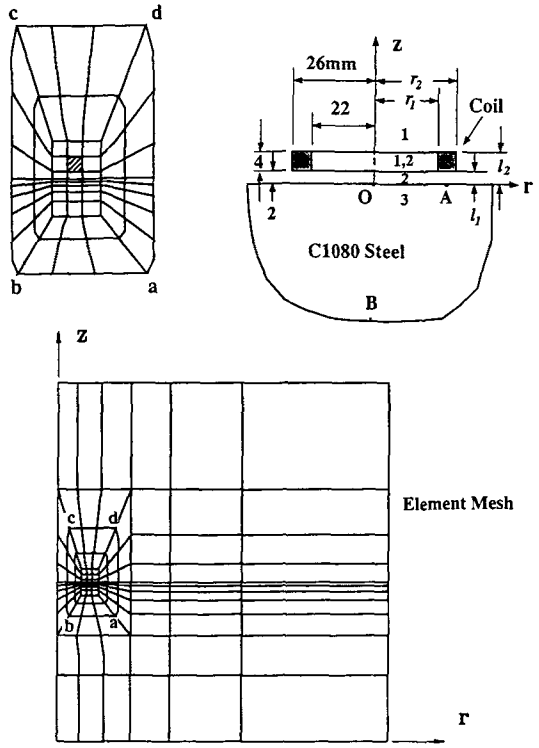

Fig. 12 Finite-element modeling for the induction heat treatment of a half-space by a coil suspended above the surface.

$\mu_r = \mu_1/\mu_0$ = relative permeability of work material.

The temperature distribution in the workpiece due to this magnetic vector potential was also obtained using a Green's function method in a manner similar to that described in the previous example. The governing equations and initial conditions for the temperature are the same as that in Example 1 in Section 4.1. The boundary conditions are

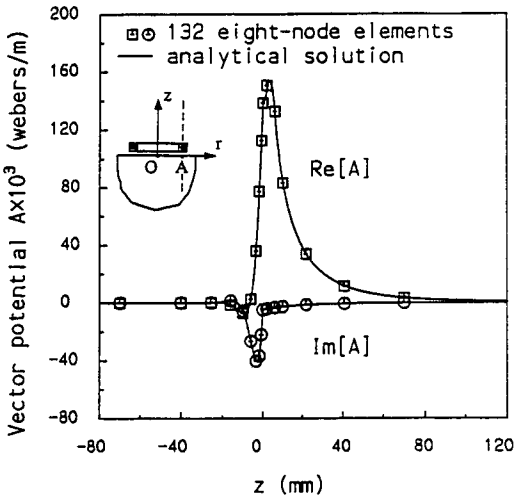

Fig. 13 Distribution of vector potential along a line parallel to the z axis through point A.

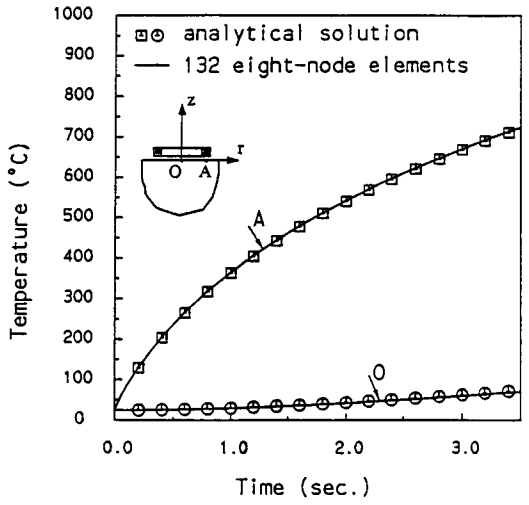

Fig. 14 Temperature histories at two points on the surface of the half-space.

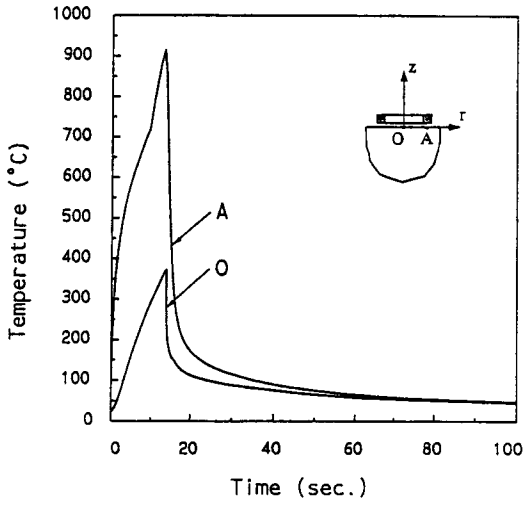

Fig. 15 Temperature histories at two points on the surface of a half-space under one coil.

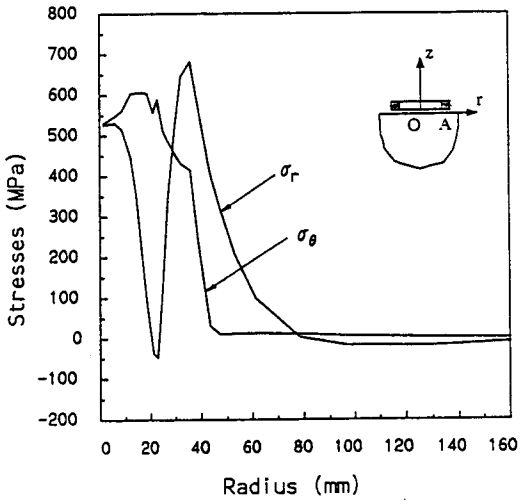

Fig. 16 Distributions of residual stresses σ_r and σ_θ, respectively, along the radial direction on the surface of the half-space at time $t = 100$ sec.

$$BCs\begin{cases}\dfrac{\partial T}{\partial r}=0 & r=0\\[2ex] \dfrac{\partial T}{\partial z}=0 & z=0\end{cases} \qquad [37]$$

From Green's function theory, the temperature distribution in the half-space for heat source $\dot{q}$ distributed throughout the solid is

$$T(r,z,t)=T_0+\frac{2\alpha}{\pi k}\int_{\tau=0}^{t}\int_{r=0}^{\infty}\int_{z=0}^{\infty}\int_{\beta=0}^{\infty}\int_{\eta=0}^{\infty}$$
$$\beta r' J_0(\beta r)J_0(\beta r')\cos(\eta z)\cos(\eta z')e^{-\alpha(\beta^2+\eta^2)(t-\tau)}$$
$$\cdot\,\dot{q}(r',-z')d\beta d\eta dr'dz'd\tau \qquad [38]$$

where $\dot{q}$ is the heat source generated by the eddy currents. For the strength of this heat source, see Example 1 in Section 4.1. The solutions obtained using finite-element and the Green's function (analytical) approaches were compared for the following conditions: Source current density and frequency in the coil being 1.2×10^{10} A/m^2 and 60 Hz, respectively. The data for the electrical conductivity, density, specific heat, and thermal conductivity were assumed to be 3×10^6 mho/m, 7500 kg/m^3, 650 J/kg · K, and 35 W/m · K, respectively. Other relevant geometric details are given in Fig. 12. The top surface of the half-space was assumed to be thermally insulated.

The distribution of the vector potential and the temperature in the half-space are shown for selected points in Fig. 13 and 14, respectively. The temperature distribution is plotted for only the first few seconds of the induction heating cycle in Fig. 14. The vector potential in the vicinity of the half-space is also shown in

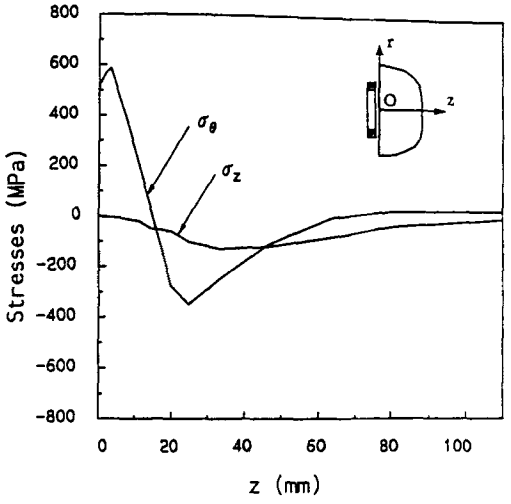

Fig. 17 Distributions of residual stresses σ_θ and σ_z, respectively, along the z axis of the half-space at time $t = 100$ sec.

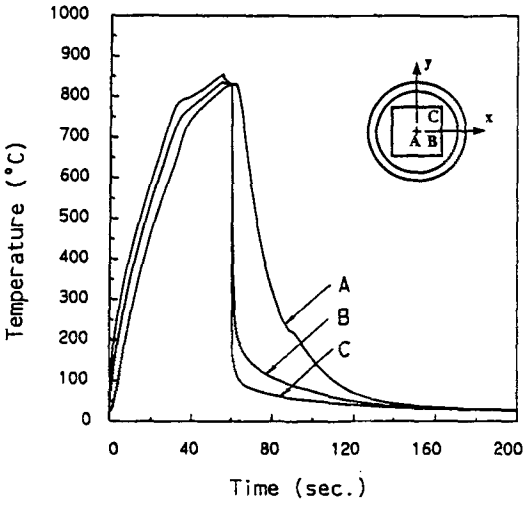

Fig. 19 Temperature histories at three points within the infinitely long square bar.

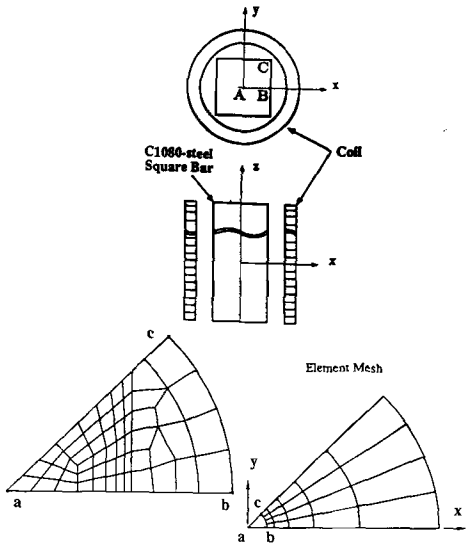

Fig. 18 Finite-element modeling for the induction heat treatment of an infinitely long 1080 steel square bar encircled by an infinitely long coil.

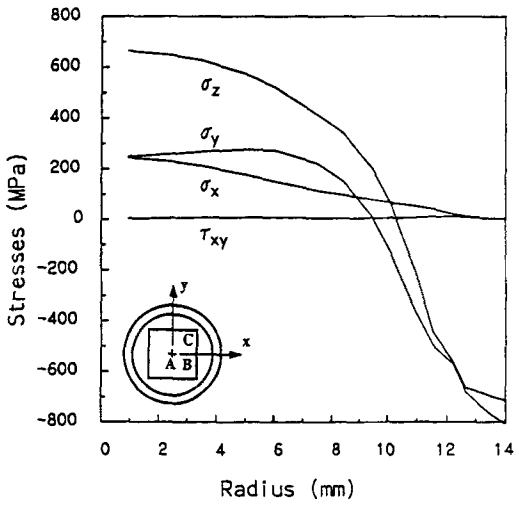

Fig. 20 Distribution of residual stresses along the x direction of the square bar.

Fig. 13. From these figures, it is clear that there is once again excellent agreement between the finite-element and the analytical solutions. This serves to validate the temperature and magnetic field calculations made using the present finite-element procedures.

The finite-element simulation of a complete cycle of the induction heat treatment of the half-space was also carried out. The cycle consisted of heating the workpiece surface inductively for 13.5 sec using the same current density as above, followed by air cooling for 0.5 sec, and then quenching to a room temperature of 25 °C in 6% UCON quenchant. The quenchant was assumed to be applied to the surface of the half-space. The variation of the heat transfer coefficient with temperature for the 6% UCON quenchant was assumed from Fig. 6. For this simulation, the thermophysical and mechanical properties of 1080 steel were assumed to be temperature dependent as described earlier, and the Curie phase transition was also included in the modeling of the magnetic field.

Three finite-element meshes (132, 164, and 216 elements, respectively) were used to model this problem to observe that the 132-element mesh generated converged results. Also, meshes coarser than 132 elements were not found to be accurate enough. Thus, the 132-element mesh, as shown in Fig. 12, was used.

Figure 15 shows the temperature distribution at two different points on the surface of the half-space during the heat treatment cycle. The discontinuity in the temperature gradient with the onset of the Curie transition is once again clearly seen in the temperature history of point A in Fig. 15. Figure 16 shows the distributions of residual stresses σ_r and σ_θ, respectively, along the

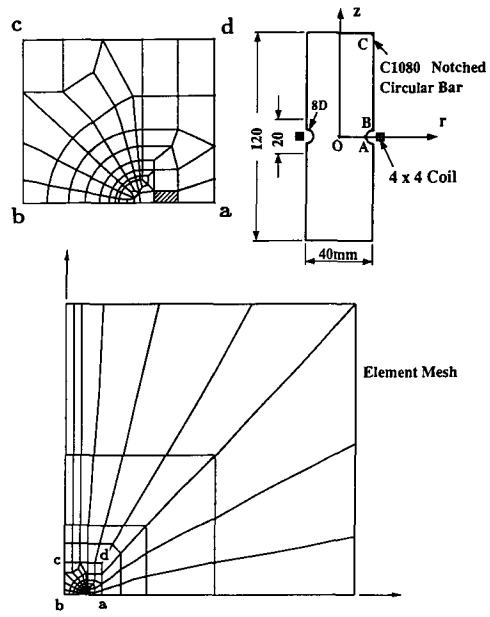

Fig. 21 Finite-element modeling for the induction heat treatment of a circular notched bar of 1080 steel by a single coil.

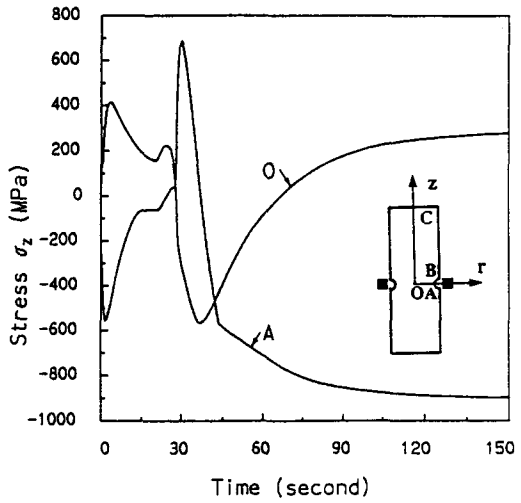

Fig. 23 Histories of axial stresses at two points of the notched circular bar during heat treatment.

radial direction on the surface of the half-space at time $t = 100$ sec. Figure 17 shows the distributions of residual stresses σ_θ and σ_z, respectively, along the z axis of the half-space at time $t = 100$ sec. These stresses were of course induced by the heat treatment process. It is interesting to note that, on the surface of the half-space in Fig. 16, there are substantial point-to-point variations in the radial and hoop residual stresses, especially in the neighborhood of the coil. The present coil configuration obviously needs to be improved for the practical heat treatment of the half-space.

4.3 *Induction Heat Treatment of an Infinitely Long 1080 Steel Square Bar Encircled by an Infinitely Long Coil*

To demonstrate the capability of the present finite-element program to simulate two-dimensional plane-strain problems, the

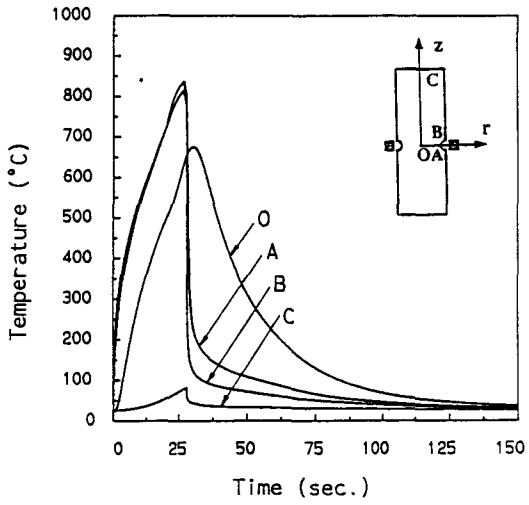

Fig. 22 Temperature histories at four different points of the notched circular bar during the induction heat treatment process.

induction heat treatment of an infinitely long square bar of 1080 steel surrounded by an infinitely long circular coil was carried out. Figure 18 shows the geometry of the problem. The inner and outer radii of the coil were 22 and 26 mm, respectively, and the bar was assumed to have a cross section of 28.28 by 28.28 mm square. The source current in the coil was assumed to be 6×10^8 A/m, varying sinusoidally at a frequency of 60 Hz. The square bar was heated for 55 sec, subjected to 5 sec of air cooling, and then quenched in 6% UCON quenchant. A mesh with 74 isoparametric eight-node elements was used, as shown in Fig. 18. The material properties for the 1080 carbon steel were assumed to be temperature dependent and the same as in the previous examples. The convective heat transfer coefficients for air and UCON quenchant (see Fig. 6) were also the same as in the earlier examples.

Three finite-element meshes (68, 74, and 160 elements, respectively) were used to model this problem to observe that the 74-element mesh generated converged results. Also, meshes coarser than 74 elements were not found to be accurate enough. Thus, the 74-element mesh, as shown in Fig. 18, was used.

Figure 19 shows the finite-element results for the temperature histories of three different points in the square bar. Again, the discontinuities in the temperature gradient with the onset of the Curie phenomenon are clearly evident in the heating cycle of Fig. 19. Figure 19 shows that the temperature at the surface and the center of the bar at the end of the heating cycle is in excess of 800 °C, which indicates that the whole bar would be austenitized before the quench. On quenching, the austenite transforms to martensite or pearlite depending on the cooling rates at any given point. The residual stresses, as induced by the induction heat treatment process, are shown in Fig. 20. The residual stress distribution shown here is very similar to the corresponding stresses calculated in a circular bar whose cross section inscribes the square and that has been subjected to a similar heat treatment cycle.[12] This serves as a rule-of-thumb check for the stress calculations. The broad features of the residual stress distribution, such as all of the stresses being compressive at the surface and predominantly tensile in the interior, are in qualitative agree-

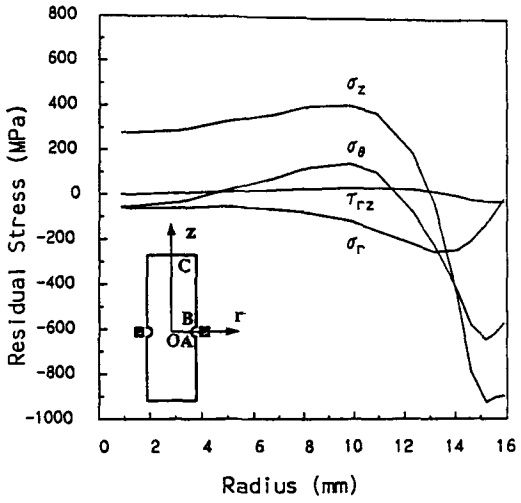

Fig. 24 Distribution of residual stresses along the radius OA of the heat treated bar.

ment with what is experimentally observed for such a heat treatment cycle. The zone of surface residual compression in the y- and z-directional stresses is found to extend to a depth of approximately 5 mm from the surface in Fig. 20. Of course, the tensile stresses in the interior make the central regions of the square bar prone to failures when subjected to external loads.

4.4 *Induction Heat Treatment of a Finite 1080 Steel Circular Notched Bar*

The last example considers the simulation of the induction heat treatment of a notched circular bar by a single coil. Many engineering components such as crankshafts, camshafts, etc., contain fillets and notches that are potential zones of failure because of the stress concentrations that occur in such areas. Local induction hardening of these regions to introduce residual compressive stresses or increase the hardness can often be used to reduce the probability of failure in such regions.

Figure 21 shows the geometrical configuration for the simulation of heat treatment of a 1080 steel bar of circular cross section containing a single semicircular notch. The bar was assumed to be 120 mm long and the coil surrounded the notched area. The circular coil had a square cross section of 4 by 4 mm. The finite-element mesh consisted of 115 isoparametric eight-node elements. A sinusoidally varying source current of density 9.5×10^9 A/m^2 with a frequency of 60 Hz was applied for 27 sec to heat the notched area; the bar was then subjected to air cooling for 1 sec and then quenched on cylindrical surfaces in a 6% UCON quenchant. The material properties for the 1080 steel and the quenchant were the same as in the previous examples.

Three finite-element meshes (94, 115, and 220 elements, respectively) were used to model this problem to observe that the 115-element mesh generated converged results. Also, meshes coarser than 115 elements were not found to be accurate enough. Thus, the 115-element mesh, as shown in Fig. 21, was used.

Figure 22 shows the temperature histories at selected points in the bar during the heat treatment cycle. From this figure, it is observed that the surface region of the notch has exceeded the austenitizing temperature before quenching began. Figure 23 shows the time evolution of the axial stresses at two points of the notched region during the heat treatment process. The distribution of residual stresses along the radius OA of the notched bar is shown in Fig. 24. At point A where the elastic stress concentration is the greatest, the residual axial stress has a large compressive value of about 900 MPa. The compressive stress region extends to a depth of about 4 mm in Fig. 24. The compressive residual stress would be beneficial to reducing failures from the notch. It is clear that the localized induction heat treatment has led to a zone of high residual compressive stress in the axial direction at the root of the notch. Furthermore, the simulation also showed that the material near the notch root is mostly martensite whose yield stress is in excess of 1000 MPa.

5 Conclusions

The residual stresses, temperature distributions, and the magnetic field developed during the induction heat treatment of 1080 steel bar have been calculated using a finite-element formulation and solution procedure. The principal features of this formulation include the incorporation of the Curie phase transition in the calculation of the magnetic field during heating, the use of nucleation and rate equations to describe the nonisothermal phase transformations taking place in 1080 steel during quenching, and temperature-dependent material properties. Four different examples were analyzed to validate the present formulation and to demonstrate its predictive capabilities. Analytical solutions using Green's function methods were derived for the magnetic field and temperature distributions in an infinitely long 1080 steel cylinder encircled by a single coil and in a half-space suspended below a coil. These enabled validation of the magnetic field and temperature calculations. Analysis of the induction heat treatment of steel cylinders of square and circular cross sections and a notched steel bar are of practical relevance to engineering applications such as the heat treatment of solid piston pins and camshafts used in engines.

Ongoing work is directed toward controlled quenching and induction heat treatment experiments to further validate the computational results and to extend the program to treat more complex geometries. Furthermore, the feasibility of using the finite-element procedures to efficiently design heat treatment parameters *a priori* for obtaining specified residual stress distributions and microstructure pattern in steels is being investigated.

Acknowledgments

This work was supported by grants from the National Science Foundation (CDR 8803017) to the Engineering Research Center for Intelligent Manufacturing Systems and the Computer Integrated Design Manufacturing and Automation Center (CIDMAC) at Purdue University. The authors wish to thank Wayne Eckerle, Bill Grant, Carl Mussoulf, Ted Winterrowd (Cummins Engine Co.), Bob Kobylarz, Tom Strong, Greg Williamson, and Tim Witte (Atlas Co.) for valuable discussions at various stages of the study. The authors also acknowledge the guidance of the NSF ERC Program Director Fred Betz.

Appendix 1

The solutions of the vector potential for the infinitely long cylinder encircled by a delta coil are

$$A^{(1)}(r,z-z_0)=\frac{\mu_0 J_0}{\pi}\int_0^\infty C_1(\alpha)I_1(\alpha_1 r)r_0K_1(\alpha r_0)\cos\alpha(z-z_0)d\alpha$$

$$A^{(2)}(r,z-z_0)=\frac{\mu_0 J_0}{\pi}\int_0^\infty [C_2(\alpha)I_1(\alpha_2 r)+D_2(\alpha)K_1(\alpha_2 r)]r_0K_1(\alpha r_0)\cos\alpha(z-z_0)d\alpha$$

$$A^{(3)}(r,z-z_0)=\frac{\mu_0 J_0}{\pi}\int_0^\infty [I_1(\alpha r)+D_3(\alpha)K_1(\alpha r)]r_0K_1(\alpha r_0)\cos\alpha(z-z_0)d\alpha$$

$$A^{(4)}(r,z-z_0)=\frac{\mu_0 J_0}{\pi}\int_0^\infty [D_3(\alpha)r_0K_1(\alpha r_0)+r_0J_1(\alpha r_0)]K_1(\alpha r)\cos\alpha(z-z_0)d\alpha \quad [39]$$

where α_1, α_2, $C_1(\alpha)$, $C_2(\alpha)$, $D_2(\alpha)$, $C_3(\alpha)$, and $D_3(\alpha)$ are the same as those listed in the main text.

Appendix 2

The solutions of the magnetic vector potential for the half-space under a delta coil are

$$A^{(1)}(r,z)=\frac{\mu_0 J_0}{2}\int_0^\infty r_0J_1(\alpha r_0)J_1(\alpha r)(e^{\alpha l}+we^{-\alpha l})e^{-\alpha z}d\alpha$$

$$A^{(2)}(r,z)=\frac{\mu_0 J_0}{2}\int_0^\infty r_0J_1(\alpha r_0)J_1(\alpha r)e^{-\alpha l}(e^{\alpha z}+we^{-\alpha z})d\alpha$$

$$A^{(3)}(r,z)=\frac{\mu_0 J_0}{2}\int_0^\infty r_0J_1(\alpha r_0)J_1(\alpha r)e^{-\alpha l}(1+w)e^{\alpha_1 z}d\alpha \quad [40]$$

where $w=(\mu_r\alpha-\alpha_1)/(\mu_r\alpha+\alpha_1)$, $\alpha_1=\sqrt{\alpha^2+j\omega\mu_1\sigma_1}$, and $\mu_r=\mu_1/\mu_0$ = relative permeability of work material.

The Green's function for the temperature field within the half-space under a coil is

$$G(r,z,t\mid r',z',\tau)=\frac{2}{\pi}\int_{\beta=0}^\infty\int_{\eta=0}^\infty \beta r'J_0(\beta r)J_0(\beta r')\cos(\eta z)\cos(\eta z')e^{-\alpha(\beta^2+\eta^2)(t-\tau)}d\beta d\eta \quad [41]$$

References

1. J. Davies and P. Simpson, *Induction Heating Handbook*, McGraw-Hill, London (1979).
2. C.V. Dodd and W.E. Deeds, Analytical Solution to Eddy-current Probe Coil Problems, Report ORNL-TM-1987 (1967).
3. C.V. Dodd, Solutions to Electromagnetic Induction Problems, Report ORNL-TM-1842 (1967).
4. J. Donea, S. Giuliani, and A. Philippe, Finite Elements in the Solution of Electromagnetic Induction Problems, *Int. J. Num. Meth. Eng.*, *8*, 359-367 (1974).
5. M.V.K. Chari, Finite-Element Solution of the Eddy-current Problem in Magnetic Structures, *IEEE Trans. PAS-93*(1), 62 (1973).
6. G. Meunier, D. Shen, and J. Coulomb, Modelisation of 2D and Axisymmetric Magnetodynamic Domain by the Finite Element Method, *IEEE Trans. Magnetics*, *24*(1), 166-169 (1988).
7. R.M. Baker,Classical Heat Flow Problems Applied to Induction Billet Heating, *AIEE Trans.*, *77*, 106-112, May (1958).
8. Ph. Massé, B. Morel, and Th. Breville, A Finite Element Prediction Correction Scheme for Magneto-thermal Coupled Problem during Curie Transition, *IEEE Trans. Magnetics*, *21*(5), 1871-1873 (1985).
9. M. Melander, Theoretical and Experimental Study of Stationary and Progressive Induction Hardening, *J. Heat Treat.*, *4*, 145-166 (1985).
10. J.D. Lavers, Numerical Solution Methods for Electroheat Problems, *IEEE Trans. Magnetics*, *19*(6), 2566-2572 (1983).
11. A.J. Fletcher, *Thermal Stress and Strain Generation in Heat Treatment*, Elsevier Science, London and New York (1989).
12. K.F. Wang, S. Chandrasekar, and H.T.Y. Yang, An Efficient 2D Finite Element Procedure for the Quenching Analysis with Phase Change, *ASME J. Eng. Ind.*, (1992).
13. R.P. Feynman, R.B. Leighton, and G. Sands, *The Feynman Lectures on Physics*, vol 2, Addison Wesley, New York (1962).
14. M. Avrami, Kinetics of Phase Change I, *J. Chem. Phys.*, *7*, 1103 (1939).
15. M. Avrami,Kinetics of Phase Change II, *J. Chem. Phys.*, *8*, 212 (1940).
16. P.K. Agarwal and J.K. Brimacombe,Mathematical Model of Heat Flow and Austenite-Pearlite Transformation in Eutectoid Carbon Steel Rods for Wire, *Met. Trans. B*, *12*, 121-133 (1981).
17. F.M.B. Fernandes, S. Denis, and A. Simon,Mathematical Model Coupling Phase Transformation and Temperature Evolution during Quenching of Steels, *Mater. Sci. Technol.*, *1*, 838-844 (1985).
18. D.P. Koistinen and R.E. Marburger, A General Equation Prescribing the Extent of the Austenite-Martensite Transformation in Pure Iron-Carbon Alloys and Carbon Steels, *Acta Metall.*, *7*, 59 (1959).
19. S. Denis, S. Sjöstrom, and A. Simon, Coupled Temperature, Stress, Phase Transformation Calculation Model Numerical Illustration of the Internal Stresses Evolution During Cooling of a Eutectoid Carbon Steel Cylinder, *Met. Trans. A*, *18*, 1203-1212 (1987).
20. P.D. Harvey, *Engineering Properties of Steel*, ASM, Materials Park (1982).
21. M.N. Özisik, *Heat Conduction*, John Wiley & Sons, New York (1980).